

Nonmonotonous classical magneto-conductivity of a two-dimensional electron gas in a disordered array of obstacles

N. H. Siboni,¹ J. Schluck,² K. Pierz,³ H. W. Schumacher,³ D. Kazazis,⁴ J. Horbach,^{1,*} and T. Heinzel^{2,†}

¹*Institut für Theoretische Physik II, Heinrich-Heine-Universität,
Universitätsstraße 1, 40225 Düsseldorf, Germany*

²*Institut für Experimentelle Physik der kondensierten Materie,
Heinrich-Heine-Universität, Universitätsstraße 1, 40225 Düsseldorf, Germany*

³*Physikalisch-Technische Bundesanstalt, Bundesallee 100, 38116 Braunschweig, Germany*

⁴*CNRS, Univ. Paris-Sud, Université Paris-Saclay, C2N Marcoussis, 91460 Marcoussis, France[‡]*

(Dated: June 4, 2022)

Magnetotransport measurements in combination with molecular dynamics (MD) simulations on two-dimensional disordered Lorentz gases in the classical regime are reported. In quantitative agreement between experiment and simulation, the magnetoconductivity displays a pronounced peak as a function of perpendicular magnetic field B which cannot be explained in the framework of existing kinetic theories. We show that this peak is linked to the onset of a directed motion of the electrons along the contour of the disordered obstacle matrix when the cyclotron radius becomes smaller than the size of the obstacles. This directed motion leads to transient superdiffusive motion and strong scaling corrections in the vicinity of the insulator-to-conductor transitions of the Lorentz gas.

PACS numbers: 64.60.ah, 73.23.-b, 75.47.-m

A system of non-interacting particles moving in a Poisson distributed array of identical obstacles is known as a Lorentz gas. Originally proposed for the motion of electrons in a metal¹, the Lorentz gas has developed into a universal model for transport phenomena in many types of heterogeneous media, like anomalous diffusion in colloidal and bio-systems^{2–7}, microwave-induced magnetoresistance oscillations⁸, or negative magnetoresistance in metallic and semiconductor systems^{9–14}. Versatile implementations of Lorentz gases can be realized experimentally by two-dimensional electron gases (2DEGs) exposed to a random array of obstacles. Such systems provide a high intrinsic electron mobility and the option to pattern the obstacles lithographically. A perpendicular magnetic field B tunes the cyclotron radius $R_{cy} \propto B^{-1}$ of the electronic motion, acting as an additional characteristic length scale.

Experimental studies of the magnetotransport of 2DEGs in disordered obstacle arrays have been scarce (see, e.g., Refs.^{15–19}). Especially, the magnetoconductivity $\sigma_{xx}(B)$ in a regime of high obstacle densities n^* and large magnetic field has not been systematically explored up to now. Here, n^* denotes the dimensionless number density of obstacles, $n^* = \frac{N}{A} R_{int}^2$, with N the number of obstacles, A the area of the system and R_{int} the interaction distance between an electron and an obstacle, i.e., the effective radius of the (circular) obstacles. In this letter, we present a semi-classical experimental realization of a Lorentz gas in combination with classical molecular dynamics (MD) simulations and demonstrate that the electron transport qualitatively changes if the cyclotron radius R_{cy} becomes smaller than the interaction distance R_{int} . As expected from kinetic theories, the conductivity $\sigma_{xx}(B)$ is a monotonously decaying function at low densities. For large densities and $R_{cy} \lesssim R_{int}$, however, it exhibits a maximum that moves to larger values of B

with increasing n^* . This maximum has been observed in simulations^{20,21} but it has hitherto remained unexplained and not been observed experimentally.

The magneto-transport in the 2D Lorentz gas is associated with two insulator-to-conductor transitions at high and low number density n^* of the obstacles which are due to underlying static percolation transitions^{20,21}. The location of the transition at high density is independent of the magnetic field B and located at a critical density $n_c^* = 0.359$ for a Poisson-distributed arrangement of overlapping disks: while for $n < n_c^*$ the electron exhibits diffusive transport through the void space between the obstacles, for $n > n_c^*$ the void space is disconnected into finite pockets in which the electron is trapped. The second, B -dependent localization transition occurs at a density $n_{ld,c}^*(B) < n_c^*$. It can be understood in terms of skipping orbits that the electrons, acting as tracer particles in this experimental implementation, perform around the obstacles, or clusters thereof, which localizes all particles as n^* , or the cyclotron radius R_{cy} , respectively, is decreased²⁰.

For a fixed B field, the magnetoconductivity exhibits a maximum as a function of n^* which is located at $n_{ld,c}^* < n_{max}^* < n_c^*$. This maximum is intimately related to the maximum in $\sigma_{xx}(B)$. As elucidated by our MD simulations, the line of maxima, $n_{max}^*(B)$, follows a simple law (see below) and merges with the two critical points in the limit $B \rightarrow \infty$. The change of the transport for $R_{cy} \lesssim R_{int}$ along the line $n_{max}^*(B)$ is due to a change of the motion of the tracer particles (electrons) from a diffuse scattering by the obstacles to a directed motion along the contour of the obstacle arrangement. In the limit $B \rightarrow \infty$, this directed motion completely dominates the transport and suppresses the critical slowing down at $n_{ld,c}^*$ and n_c^* . At finite but high B fields it leads to strong corrections to the scaling behavior in the vicinity of the

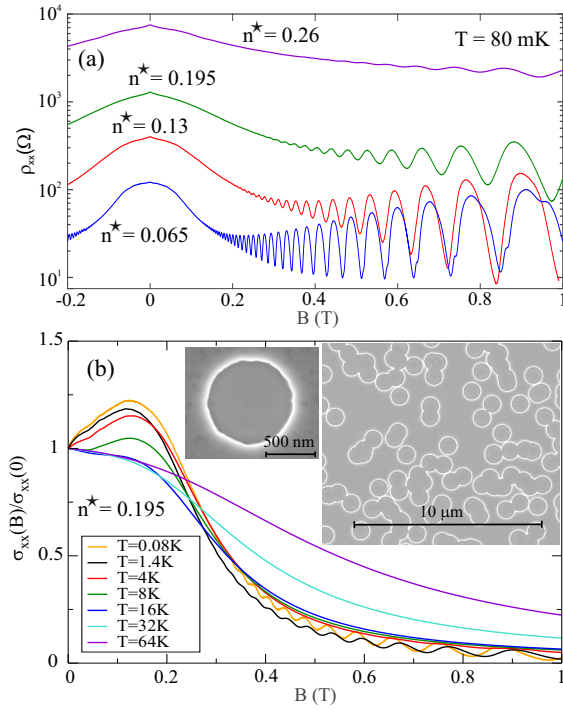


FIG. 1. (a) The longitudinal magnetoresistivities ρ_{xx} of the Lorentz gases of various obstacle densities n^* , measured at a temperature of ≈ 80 mK. (b) The magnetoconductivity $\sigma_{xx}(B)$ and its temperature dependence, as determined from the measurements for the $n^* = 0.195$ array. Insets: Scanning electron microscope picture of a Lorentz array section with $n^* = 0.195$ and magnified view of a single disk.

critical points.

Experiment. A GaAs/Al_{0.3}Ga_{0.7}As heterostructure with a 2DEG located 150 nm below the surface is used. The electron density and mobility are $n_e = 2.5 \times 10^{15} \text{ m}^{-2}$ and $340 \text{ m}^2/\text{Vs}$, respectively, corresponding to a mean free path of $31 \mu\text{m}$ at temperatures below 1 K. The repulsive Lorentz obstacles are formed by circular holes in the 2DEG. They are patterned by electron beam lithography and subsequent inductively coupled reactive ion etching. Within each array, the obstacles are nominally identical in shape and size, while their positions are Poisson distributed, with mutual overlaps allowed. All disks have a lithographic radius of 425 nm , see Fig. 1(a). From Aharonov-Bohm measurements in large magnetic fields²², we estimate the lateral depletion length to $\approx 75 \text{ nm}$ ²³, such that the effective electronic disk radius is $R_{\text{int}} \approx 500 \text{ nm}$. Besides a Hall bar without intentional obstacles, the chip contains four Lorentz arrays with disk densities $n^* = 0.065, 0.13, 0.195$, and 0.26 , respectively. The arrays have an area of $200 \mu\text{m}$ by $100 \mu\text{m}$. The mean free path due to the scattering at the disks is $4 \mu\text{m}, 2 \mu\text{m}, 1.3 \mu\text{m}$, and $1 \mu\text{m}$, respectively.

The samples were inserted in the mixing chamber of a dilution refrigerator with a base temperature of 8 mK . The electron temperature is estimated to $\approx 80 \text{ mK}$. A ^4He gas flow cryostat with a variable temperature in-

sert and a base temperature of 1.4 K is used for measurements at temperatures above 1 K . An AC current (500 nA , 17.7 Hz) is injected. The longitudinal and Hall voltages are measured at suitable probes using lock-in amplifiers.

The longitudinal magnetoresistivity $\rho_{xx}(B)$ (see Fig. 1(a)) shows a strong peak around $B = 0$ which in some arrays extends well into the range where Shubnikov-de Haas oscillations²⁴ are observed. As n^* is increased from 0.065 to 0.26 , $\rho_{xx}(0)$ increases by approximately a factor of 50 .

The longitudinal magnetoconductivity is obtained from the measured resistivity components via $\sigma_{xx}(B) = \rho_{xx}(B)/(\rho_{xx}^2(B) + \rho_{xy}^2(B))$, where $\rho_{xy}(B)$ denotes the Hall resistivity (see the supplement for the corresponding measurements). In Fig. 1(b), the thereby obtained $\sigma_{xx}(B)$ is shown for the array with $n^* = 0.195$ for various temperatures. A pronounced maximum at $B \approx 140 \text{ mT}$ is observed. It shows a weak temperature dependence and evolves at higher temperatures into a shoulder that is still visible at 32 K . This weak temperature dependence indicates a classical origin. We have observed the same phenomenology in a set of scaled samples with identical number densities but with $R_{\text{int}} = 1 \mu\text{m}$ (not shown). This behavior is in qualitative contradiction to both the Boltzmann model as well as to the Bobylev model valid for Lorentz gases with small n^* ²⁵. Rather, it is associated with the above mentioned conductivity maximum as predicted by numerical simulations for high density Lorentz gases^{20,21}.

Simulations. Classical molecular dynamics of a system of non-interacting fluid particles in a two-dimensional matrix of randomly placed obstacle particles are performed using LAMMPS²⁶ with a modified integrator to include the magnetic field. Matrix (index M) and fluid particles (F) interact via a shifted, purely repulsive Weeks-Chandler-Andersen (WCA) potential, $u_{\text{FM}}(r) = 4\epsilon [(R_{\text{int}}/r)^{12} - (R_{\text{int}}/r)^6 + 1/4]$ for $r < 2^{1/6}R_{\text{int}}$ and $u_{\text{FM}}(r) = 0$ otherwise. Here, we have set the energy parameter to $\epsilon = 0.1 \epsilon_M$ and the interaction range to $R_{\text{int}} = 0.5 \sigma_M$ where $\epsilon_M = 1.0$ and $\sigma_M = 1.0$ correspond to the energy parameter and the diameter of the obstacle particles, respectively. For the comparison between simulation and experiment exactly the same configurations of obstacles as in the experiment are implemented. For the other calculations, we use 100 statistically independent matrix structures at each number density, $n^* = \frac{N}{L^2} R_{\text{int}}^2$ with N the number of matrix particles and L the linear dimension of the simulation square.

Newton's equations of motion are integrated numerically using the velocity-Verlet algorithm²⁷ with a time step of $10^{-3}t_0$ with $t_0 := [m(\sigma_M)^2/\epsilon_M]^{1/2}$ and $m = 1.0$ the mass of a fluid particle. The particles carry a charge $e = 1$ and a mass $m = 1$, and are subjected to a uniform magnetic field B that acts perpendicular to the plane of motion. The velocity of the fluid particles is fixed to a constant magnitude $v_F = \sqrt{2}$, associated with a cyclotron radius of $R_{\text{cy}} = mv_F/(eB)$ or $R_{\text{cy}} = R_{\text{int}}/\tilde{B}$,

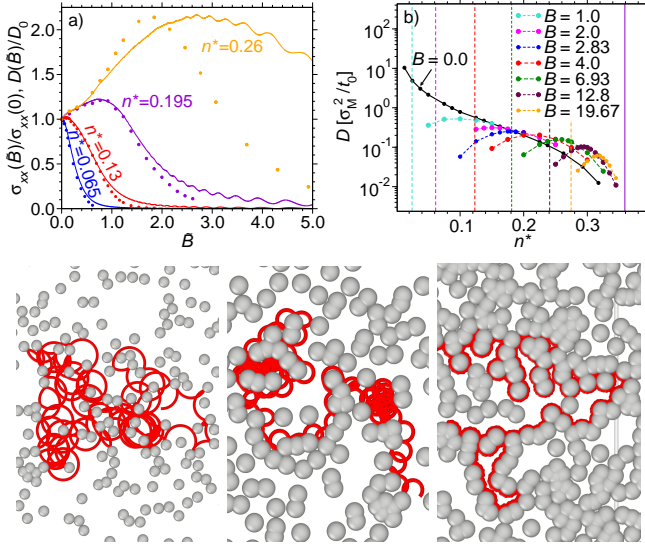


FIG. 2. (a) $\sigma_{xx}(\tilde{B})/\sigma_{xx}(0)$ from experiment (full lines) in comparison to $D(\tilde{B})/D(0)$ from simulation (full circles) for different values of n^* . (b) $D(n^*/n_c^*)$ from the simulation for different values of \tilde{B} . The vertical lines correspond to the locations of n_c^* (solid line) and $n_{ld,c}^*(\tilde{B})$ (dashed lines). The snapshots correspond to the location of the maxima in $D(n^*)$ for $\tilde{B} = 0.35, 1.41$, and 6.95 (from left to right). The trajectories are illustrated using OVITO²⁸.

with \tilde{B} being the dimensionless magnetic field $\tilde{B} = B/B_0$ (with $B_0 = \frac{mv_F}{eR_{int}}$). Between 100 and 2400 fluid particles per host structure are used for runs of up to $10^6 t_0$. For the calculation of time averages, 10 time origins per run are used, spaced equidistantly over the whole simulation time.

The conversion of units between simulation and experiment is as follows: $\sigma_M = 10^{-6}$ m (obstacle diameter), $m = 6.097 \times 10^{-32}$ kg (effective electron mass in GaAs), $t_0 = 9.226 \times 10^{-12}$ s, $e = 1.6 \times 10^{-19}$ C (electron charge), and $B_0 = 0.168$ T.

Results. For a system of non-interacting charged particles (electrons), the conductivity σ_{xx} is directly related to the self-diffusion constant D via $\sigma_{xx} = \frac{ne^2}{m} D$. Hence, we can directly compare the experimentally obtained conductivity, normalized to its value at $\tilde{B} = 0$, $\sigma_{xx}(\tilde{B})/\sigma_{xx}(0)$, to the corresponding ratio of diffusion constants from the MD simulation, $D(\tilde{B})/D(0)$. In the simulation, the self-diffusion constant can be obtained from the long-time limit of the mean-squared displacement (MSD) of a tagged particle, $\delta r^2(t)$, using the Einstein relation $D = \lim_{t \rightarrow \infty} \delta r^2(t)/4t$. Here, the MSD is defined as $\delta r^2(t) = \langle (\vec{r}(t) - \vec{r}(0))^2 \rangle$, with $\vec{r}(t)$ the position of the particle at time t and $\langle \dots \rangle$ an ensemble average.

The comparison of $\sigma_{xx}(\tilde{B})/\sigma_{xx}(0)$ from the experiment with $D(\tilde{B})/D(0)$ from the simulation is shown in Fig. 2a for different number densities. At low \tilde{B} fields, simulation and experiment are in good agreement. We note that therefore, both weak localization corrections²⁹ and

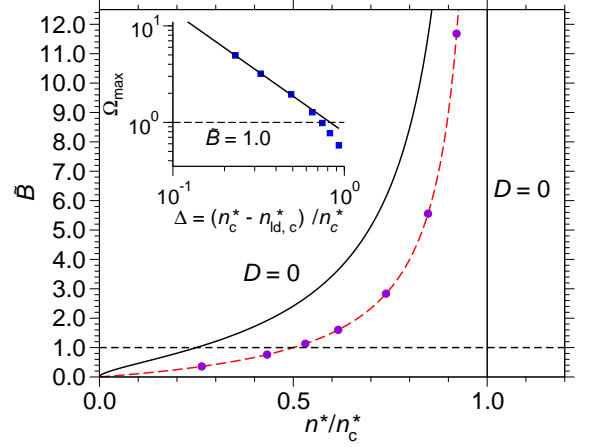


FIG. 3. Phase diagram in terms of \tilde{B} vs. n^*/n_c^* . The red dashed line is obtained from Eq. (1) and filled blue circles show \tilde{B}_{max} , as determined from the simulation (cf. Fig. 2 (b)). The inset shows Ω_{max} as function of Δ , with the solid line being a fit with $\Omega_{max} \propto \Delta^{-1.25}$ (see text).

interaction effects³⁰ can be excluded as possible origin. The experimental values are significantly larger than the ones from the simulation at high \tilde{B} fields. We tentatively attribute these deviations to a combination of quantum effects like the onset of Shubnikov-de Haas oscillations, and depinning of electrons from the obstacle clusters by the residual random disorder¹⁰. However, different from the monotonous decay of $\sigma_{xx}(\tilde{B})/\sigma_{xx}(0)$ and $D(\tilde{B})/D(0)$ at low densities, a maximum occurs at large densities (see, e.g. the results for $n^* = 0.195$ where simulation and experiment are in very good agreement around the maximum).

To get further insight into the nature of this change we plot in Fig. 2(b) the diffusion constant from the simulation as function of number density, $D(n^*)$, for different values of \tilde{B} , including $\tilde{B} = 0$. At a given finite value of \tilde{B} , the diffusion coefficients vanish at the critical densities n_c^* and $n_{ld,c}^*(\tilde{B}) < n_c^*$. Therefore, at a given value of \tilde{B} , the function $D(n^*)$ exhibits a maximum in the interval $[n_{ld,c}^*(\tilde{B}), n_c^*]$. The snapshots in Fig. 2 show typical trajectories for different densities corresponding to the maxima in $D(n^*)$ at $\tilde{B} = 0.35, 1.41$ and 6.95 from left to right (cf. corresponding movies in the supplementary material). These snapshots indicate a qualitative change of the motion around $\tilde{B} = 1$, from a diffuse scatter of the tracer particle by the obstacle for $\tilde{B} \ll 1$ to a directed motion along the contour of the obstacle network for $\tilde{B} \gg 1$. The trajectory at $\tilde{B} = 1.41$ indicate a mixture of diffuse scattering and directed motion.

The phase diagram in Fig. 3 shows \tilde{B} vs. n^*/n_c^* , with the two lines of critical points at low and high density. While the critical points at high density are independent of \tilde{B} at $n^*/n_c^* = 1$, the low density critical points are located at $\tilde{B}_{ld,c} = \left(\sqrt{n_c^*/n^*} - 1 \right)^{-1}$ ²⁰. The dashed red line in between the two critical lines in Fig. 3 corre-

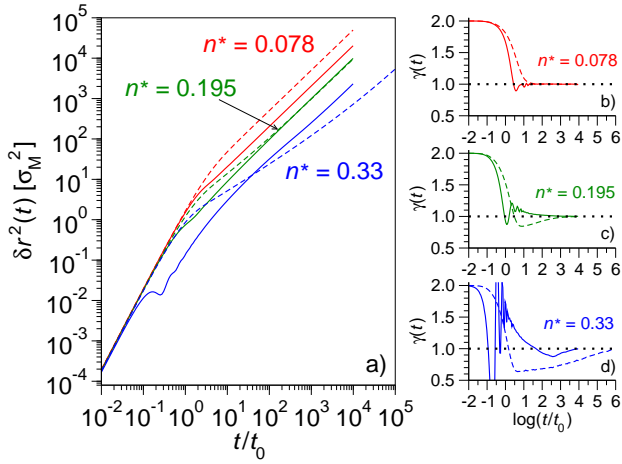


FIG. 4. a) MSDs, $\delta r^2(t)$, for the densities $n^* = 0.078$, 0.195 , and 0.33 . The dashed lines are for $\tilde{B} = 0$, while the solid lines correspond to the location of maximal diffusion at $\tilde{B} = 0.36$, 1.02 , and 7.09 , respectively. Panels b), c), and d) show the local exponents $\gamma(t)$, corresponding to the MSDs in a).

sponds to the points of maximal diffusion. Its form can be understood as follows: The density $n_{\max}(\tilde{B})$ at which the diffusion coefficient is maximal is associated with two limiting cases. The maximum vanishes towards $\tilde{B} \rightarrow 0$, i.e. $n_{\max}(\tilde{B} \rightarrow 0) = 0$, and it should coincide with n_c^* in the limit $\tilde{B} \rightarrow \infty$ (then $R_{cy} = 0$ and $n_c^* = n_{ld,c}^*$). A function that interpolates between these two limiting cases is $n_{\max}^* = n_c^* R_{int} (R_{int} + R_{cy})^{-1}$. When this expression is solved for \tilde{B} , one obtains the following law for the density dependence of the reduced magnetic field at maximal diffusion:

$$\tilde{B}_{\max} = (n_c^*/n^* - 1)^{-1} \quad (1)$$

The points that are on the maximal diffusion curve in Fig. 3 are directly obtained from the data in Fig. 2b, confirming that Eq. (1) indeed holds. Along the line of maxima, the transport of the tracer particle changes around $\tilde{B} = 1$. This can be inferred from the inset in Fig. 3 where the ratio of the diffusion constant at the maximum to that at $\tilde{B} = 0$ at the corresponding density, $\Omega_{\max} = D_{\max}(B)/D(n_{\max}^*, \tilde{B} = 0)$, is plotted as a function of the distance between the two critical lines at a given value of \tilde{B} , $\Delta = (n_c^* - n_{ld,c}^*)/n_c^*$. For $\Delta \lesssim 0.7$, the ratio Ω_{\max} is larger than 1.0 (corresponding also to $\tilde{B} > 1.0$), and the data can be fitted with a power law, $\Omega_{\max} \propto \Delta^{-1.25}$, indicating a divergence of this ratio towards $\tilde{B} \rightarrow \infty$. As a consequence, one expects at least strong corrections to the asymptotic critical behavior for large \tilde{B} fields and, in the limit $\tilde{B} \rightarrow \infty$, where the two critical points meet, the diffusion constant does not vanish but becomes infinite.

On a microscopic scale, the qualitative change of the tracer particle motion around $\tilde{B} = 1$ can be analyzed in terms of MSDs. Figure 4a displays MSDs at three different states of maximal diffusion, (n_{\max}^*, \tilde{B}) (cf. the snap-

shots in Fig. 2 at the same states). Also included are MSDs for $\tilde{B} = 0$ (dashed lines) at the corresponding densities. The onset of a directed motion along the contour of the obstacles is associated with a superlinear regime in the MSD at intermediate times for $t \gtrsim 3t_0$. This is especially evident from the behavior of the local exponent of the MSD, $\gamma(t) = d \log(\delta r^2(t))/d \log(t)$, which is shown in Figs. 2b)-d) for the three different densities. At $n^* = 0.078$ the diffusive regime is already reached around $t = 10t_0$ and the diffusion for $\tilde{B} = 0.36$ is slightly slower than for $\tilde{B} = 0$ due to the existence of the low-density critical point in the former case. At $n^* = 0.195$, there is a superlinear regime for $1.0t_0 \lesssim t \lesssim 100t_0$ at $\tilde{B} = 1.02$, while in the case of $\tilde{B} = 0$, a sublinear regime is seen in the same time range. A similar effect, albeit much more pronounced, is present for $n^* = 0.33$. Here, the $\tilde{B} = 0$ curve shows an extended sublinear regime over about 2-3 orders of magnitude due to the vicinity of the critical density n_c^* . This regime is almost suppressed for $\tilde{B} = 7.09$; instead a pronounced superlinear regime and a faster transition towards normal diffusion is observed. This indicates that particularly in a dense matrix the application of a magnetic field $\tilde{B} \gg 1.0$ leads to a very efficient exploration of the matrix due to the directed motion along the contour of the obstacle matrix.

Summary and conclusions. Using a combination of experiment and simulation, we have studied the magneto-transport through two-dimensional disordered Lorentz gases in the classical regime. Our focus was on the non-monotonous behavior of the conductivity/diffusion which is observed for magnetic fields $\tilde{B} \gtrsim 1.0$. These features cannot be described by any of the existing kinetic theories. We emphasize that the system under study is also related to the active motion of microswimmers⁷ and thus has a more general relevance. The threshold $\tilde{B} \approx 1.0$ marks the point where the cyclotron radius becomes smaller than the obstacle radius. This leads to the change in the motion of the tracer particle from a diffuse scatter by the obstacles to a directed motion along the obstacle contour. The latter directed motion is associated with an intermediate superlinear regime in the MSD that becomes more pronounced with increasing \tilde{B} .

We have shown that one can draw a line of maximal diffusion into the phase diagram that follows the law given by Eq. (1). Along this line, the diffusion constant ratio Ω_{\max} (see above) diverges in the limit $\tilde{B} \rightarrow \infty$ (note that in this limit the two critical lines intersect and thus $n_c^* = n_{ld,c}^*$). Thus, in the limit $B \rightarrow \infty$ the directed motion dominates the transport and leads to a divergence instead of a vanishing of the diffusion coefficient. For finite \tilde{B} , at least strong scaling corrections are expected in the vicinity of the two critical points. Whether there is even a continuous change of the universality class with respect to the two critical points with increasing \tilde{B} is a subject of forthcoming studies.

Acknowledgments. We thank Thomas Franosch and Herbert Spohn for useful discussions. The authors acknowledge financial support by the German DFG, FOR

1394 (grant HO 2231/7-2). Computer time at the ZIM

of the University of Düsseldorf is also gratefully acknowledged.

* horbach@thphy.uni-duesseldorf.de

† Thomas.Heinzel@hhu.de

‡ Present address: Laboratory for Micro- and Nanotechnology, Paul Scherrer Institute, 5232 Villigen-PSI, Switzerland.

- ¹ H. Lorentz, Proc. R. Acad. Sci. Amsterdam **7**, 438 (1905).
- ² F. Höfling, T. Franosch, and E. Frey, Phys. Rev. Lett. **96**, 165901 (2006).
- ³ M. R. Horton, F. Höfling, J. O. Rädler, and T. Franosch, Soft Matter **6**, 2648 (2010).
- ⁴ F. Höfling and T. Franosch, Rep. Progr. Phys. **76**, 046602 (2013).
- ⁵ T. O. E. Skinner, S. K. Schnyder, D. G. A. L. Aarts, J. Horbach, and R. P. A. Dullens, Phys. Rev. Lett. **111**, 128301 (2013).
- ⁶ S. K. Schnyder, M. Spanner, F. Höfling, T. Franosch, and J. Horbach, Soft Matter **11**, 701 (2015).
- ⁷ M. Zeitz, K. Wolff, and H. Stark, Eur. Phys. J. E **40**, 23 (2017).
- ⁸ Y. M. Beltukov and M. I. Dyakonov, Phys. Rev. Lett. **116**, 176801 (2016).
- ⁹ B. L. Altshuler, D. E. Khmelnitsky, A. I. Larkin, and P. Lee, Phys. Rev. B **22**, 5142 (1980).
- ¹⁰ A. D. Mirlin, D. G. Polyakov, F. Evers, and P. Wölfle, Phys. Rev. Lett. **87**, 126805 (2001).
- ¹¹ D. G. Polyakov, F. Evers, A. D. Mirlin, and P. Wölfle, Phys. Rev. B **64**, 205306 (2001).
- ¹² A. Dmitriev, M. Dyakonov, and R. Jullien, Phys. Rev. Lett. **89**, 266804 (2002).
- ¹³ A. Dmitriev, A. D. Mirlin, D. G. Polyakov, and M. A. Zudov, Rev. Mod. Phys. **84**, 1709 (2012).
- ¹⁴ L. Bockhorn, I. V. Gornyi, D. Schuh, C. Reichl, W. Wegscheider, and R. J. Haug, Phys. Rev. B **90**, 165434 (2014).
- ¹⁵ G. M. Gusev, P. Basmaji, Z. D. Kvon, L. V. Litvin, Y. Nastaushchev, and A. I. Toropov, J. Phys.: Condens. Matter **6**, 73 (1994).
- ¹⁶ K. Tsukagoshi, S. Wakayama, K. Oto, S. Takaoka, K. Murase, and K. Gamo, Phys. Rev. B **52**, 8344 (1995).
- ¹⁷ G. Nachtwei, G. Lütjering, D. Weiss, Z. H. Liu, K. von Klitzing, and C. T. Foxon, Phys. Rev. B **55**, 6731 (1997).
- ¹⁸ G. Nachtwei, Z. H. Liu, G. Lütjering, R. R. Gerhardts, D. Weiss, K. von Klitzing, and K. Eberl, Phys. Rev. B **57**, 9937 (1998).
- ¹⁹ O. Yevtuchenko, G. Lütjering, D. Weiss, and K. Richter, Phys. Rev. Lett. **84**, 542 (2000).
- ²⁰ A. Kuzmany and H. Spohn, Phys. Rev. E **57**, 5544 (1998).
- ²¹ W. Schirmacher, B. Fuchs, F. Höfling, and T. Franosch, Phys. Rev. Lett. **115**, 240602 (2015).
- ²² Y. Iye, M. Ueki, A. Endo, and S. Katsumoto, J. Phys. Soc. Japan **73**, 3370 (2004).
- ²³ J. Schluck, S. Fasbender, T. Heinzel, K. Pierz, H. W. Schumacher, D. Kazazis, and U. Gennser, Phys. Rev. B **91**, 195303 (2015).
- ²⁴ T. Ando, A. B. Fowler, and F. Stern, Rev. Mod. Phys. **54**, 437 (1982).
- ²⁵ A. V. Bobylev, F. A. Maaø, A. Hansen, and E. H. Hauge, Phys. Rev. Lett. **75**, 197 (1995).
- ²⁶ S. Plimpton, J. Comp. Phys. **117**, 1 (1995).
- ²⁷ K. Binder, J. Horbach, W. Kob, W. Paul, and F. Varnik, J. Phys.: Condens. Matter **16**, S429 (2004).
- ²⁸ A. Stukowski, Mod. Simul. Mater. Sci. Eng. **18**, 015012 (2010).
- ²⁹ B. L. Altshuler, A. G. Aronov, and D. E. Khmelnitsky, J. Phys. C **15**, 7367 (1982).
- ³⁰ P. S. Alekseev, Phys. Rev. Lett. **117**, 166601 (2016).